Check for updates

Controlling factors of latitudinal distribution of dissolved organic matter in the upper layers of the Indian Ocean

M. Shigemitsu[1]* , K. Sasaoka[1], M. Wakita[2], T. Yokokawa[3], T. Hashioka[4], K. Arulananthan[5] and A. Murata[1]

Abstract

We studied chromophoric (CDOM) and fluorescent (FDOM) dissolved organic matter (DOM) and dissolved organic carbon in surface waters to determine the factors controlling the geographical distribution of DOM along two meridional transects in the Indian Ocean. For CDOM, we calculated the absorption coefficients, spectral slope, and absorption coefficient ratio from the observed absorption spectra. For FDOM, we calculated the biological (BIX) and humification (HIX) indices from the excitation emission matrices (EEMs); parallel factor analysis of the EEMs identified three fluorescent components, i.e., two humic-like and one protein-like. Using these DOM parameters, a factor analysis extracted fewer latent variables than the observed variables to account for the geographical distributions. We obtained three factors (F1, F2, and F3), which explained ~84% of the variance in the observed data. From the factor loadings, F1, F2, and F3 were interpreted as the effects of net primary production-derived DOM and its horizontal transport, photodegradation, and vertical transport by physical processes. We characterized seven marine biogeochemical provinces by factor scores. F1 scores gradually decreased from the northernmost to the Antarctic province, with a small maximum around the subtropical front. F2 scores were highest in the subtropical province and decreased in both the northward and southward directions. F3 scores were high in the Antarctic and northernmost provinces, and lowest in the subtropical province. Only BIX was insufficiently explained by these factors. BIX was highest in the northern part of the subtropical province, where photodegradation of DOM was the most intense. This suggests that the possible interaction between photodegradation, autochthonous production, and reworking by heterotrophic bacteria of DOM occurs in the subtropical province.

Keywords　FDOM, CDOM, DOC, Surface mixed layer, Indian Ocean

*Correspondence:
M. Shigemitsu
ma-shige@jamstec.go.jp
[1] Physical and Chemical Oceanography Research Group, Global Ocean Observation Research Center, Research Institute for Global Change, Japan Agency for Marine-Earth Science and Technology (JAMSTEC), 2-15 Natsushima-cho, Yokosuka, Kanagawa 237-0061, Japan
[2] Mutsu Institute for Oceanography, Research Institute for Global Change, Japan Agency for Marine-Earth Science and Technology (JAMSTEC), 690 Kitasekine Sekine, Mutsu, Aomori 035-0022, Japan
[3] Super-Cutting-Edge Grand and Advanced Research Program, Institute for Extra-Cutting-Edge Science and Technology Avant-Garde Research, Japan Agency for Marine-Earth Science and Technology (JAMSTEC), Yokosuka, Japan
[4] Marine Ecosystem Research Group, Earth Surface System Research Center, Japan Agency for Marine-Earth Science and Technology (JAMSTEC), Yokosuka, Japan
[5] National Institute of Oceanography and Marine Sciences, National Aquatic Resources Research and Development Agency, Colombo, Sri Lanka

1 Introduction

Globally, the export of dissolved organic matter (DOM) from the ocean surface to the interior accounts for approximately 20% of the biological pump (Roshan and DeVris 2017). However, very few current climate models consider marine DOM dynamics. This is most likely because information regarding DOM dynamics in surface waters is scarce, and most marine DOM is refractory to centennial-to-millennial turnover time (Hansell 2013). The contribution of DOM to biological pumps varies regionally (Roshan and DeVries 2017) and is expected to change with global warming (Lønborg et al. 2020). Thus, large-scale investigations of DOM in the ocean are becoming increasingly important to thoroughly understand the mechanisms controlling the surface DOM distribution and to properly incorporate DOM dynamics into climate models. Various biogeochemical sources and sinks of DOM exist in surface waters. Autochthonous DOM sources are primarily derived from extracellular release (Wood and Van Valen 1990) and autolysis (Veldhuis et al. 2001) by phytoplankton. This is followed by other processes such as sloppy feeding (Møller 2007), excretion (Thibodeau et al. 2020), and defecation (Lampert 1978) by zooplankton; bacterial production (Kawasaki and Benner 2006); and viral lysis (Middelboe and Lyck 2002). DOM sinks are mainly biodegradation by heterotrophic prokaryotes (del Giogio and Duarte 2002) and photodegradation (Andrews et al. 2000). The net balance between the sources and sinks, as well as physical ocean processes, including advection and mixing determines the local tendencies of DOM in the surface water and its spatial distribution.

Dissolved organic carbon (DOC) is typically measured to quantify the amount of DOM. However, DOC does not provide specific information regarding the DOM quality. Considering the above-mentioned processes related to DOM dynamics, measuring DOC alone is insufficient to describe the dynamics of DOM in surface water; therefore, information regarding DOM quality is needed. To this end, measuring the optical properties (i.e., absorbance and fluorescence) of DOM is the most suitable for large-scale DOM observations because of their high-throughput and low-cost advantages over other measurements for determining molecular, elemental, and/or isotopic properties (Medeiros et al. 2015; Broek et al. 2020). Chromophoric dissolved organic matter (CDOM) is a DOM fraction that absorbs light in the ultraviolet (UV) and visible regions. The absorption coefficient, spectral slope, and absorption coefficient ratio at different wavelengths can be used to infer the processes that affect the surface DOM composition (Iuculano et al. 2019). A fraction of CDOM fluoresces and is called fluorescent dissolved organic matter (FDOM), and treating

the excitation–emission matrix (EEM) with parallel factor analysis (PARAFAC), as well as the ratio of fluorescent intensity of some pairs of excitation and emission wavelengths, can be used to clarify the variability in DOM composition in surface waters (Heller et al. 2013; Kowalczuk et al. 2013; Catalá et al. 2016; Loginova et al. 2016; Yamashita et al. 2017). The above studies verified that CDOM and FDOM-related parameters are useful for obtaining information regarding the DOM composition.

To date, several studies have addressed the optical properties of DOM or DOC in surface water at basin or global scales (Hansell 2009; Heller et al. 2013; Kowalczuk et al. 2013; Catalá et al. 2016; Yamashita et al. 2017; Iuculano et al. 2019). Kowalczuk et al. (2013) and Heller et al. (2013) examined CDOM and FDOM distributions along meridional transects in the Atlantic; Yamashita et al. (2017) recorded observations of FDOM within wide latitudinal and longitudinal ranges in the Pacific. Although Catalá et al. (2016) and Iuculano et al. (2019) used global observations of FDOM and CDOM, respectively, the observations in the Indian Ocean were confined to the subtropical region. Kim et al. (2020) and Shigemitsu et al. (2020) observed the meridional distributions of FDOM in the Indian Ocean but mainly targeted processes occurring in deep (> 250 m) rather than upper waters. Hansell (2009) reported DOC distributions along the transects from the northern end to ~ 40° S in the Central Indian Ocean, in the Arabian Sea (AS), and in the Bay of Bengal (BoB). Based on DOC measurements along the transects, they arrived at the following conclusion with respect to the surface waters: (1) In the Central Indian Ocean, DOC concentrations are high in warm and low-latitude waters but low in cold and high-latitude waters. They suggested that the former is due to reduced vertical mixing and the latter due to greater vertical mixing. (2) In the AS surface waters, DOC concentrations were in a range of ~ 70–80 μmol/kg in summer and ~ 75–90 μmol/kg in winter, showing seasonal variabilities in DOC budgets. (3) In the BoB, high DOC concentrations (> 75 μmol/kg) were found in the surface waters of the northernmost part of the section, probably affected by rivers and tending to decrease with decreasing latitude. Regardless, the Indian Ocean is the least-examined basin in terms of surface DOM quality, although the DOC distributions as DOM quantity have been determined to some extent.

In this study, we obtained large-scale observations of the optical properties of DOM (CDOM and FDOM) and DOC along the meridional transects in the Indian Ocean. The meridional transects range from the northern to the southern end of the Indian Ocean (Fig. 1), where basin-scale information on surface DOM in terms of both amount and composition is scarce. As such, our objectives in this study were to: (1) clarify the meridional
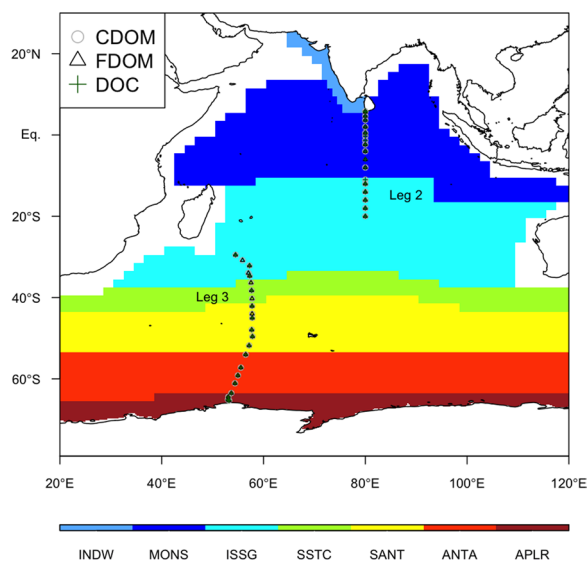
Fig. 1 Map of sampling sites. The northern transect is Leg 2 and the southern transect is Leg 3. According to Longhurst (1998), the seven biogeochemical provinces encountered in this study are shown in colors: INDW (steel blue), Western India Coastal; MONS (blue), Indian Monsoon Gyres; ISSG (light blue), Indian South Subtropical Gyre; SSTC (yellow green), South Subtropical Convergence; SANT (yellow), Subantarctic Water Ring; ANTA (orange), Antarctic; APLR (brown), Austral Polar provinces. Gray circles represent sites where CDOM measurements were obtained, black triangles represent sites for FDOM measurements, and green crosses represent DOC measurements

distributions of the optical properties of DOM and DOC in the surface waters of the Indian Ocean and (2) obtain a synoptic view of the factors controlling the meridional distributions of DOM using the observations.

2 Materials and Methods

2.1 Sampling

We obtained observations and samples through global ocean ship-based hydrographic investigations program (GO-SHIP) cruises aboard the R/V Mirai (MR19-04, Legs 2 and 3) (Fig. 1). Leg 2 covered the northern transect (December 5–27, 2019) and Leg 3 covered the southern transect (December 29, 2019–January 22, 2020). The cruises for both legs were conducted from north to south. Both legs covered the seven biogeochemical provinces (BGCPs) proposed by Longhurst (1998): the Western India Coastal (INDW), Indian Monsoon Gyres (MONS), Indian South Subtropical Gyre (ISSG), South Subtropical Convergence (SSTC), Subantarctic Water Ring (SANT), Antarctic (ANTA), and Austral Polar (APLR) provinces. In this study, we used measurements obtained above a depth of 250 m, although we collected seawater samples from depths between 10 and 10 m above the bottom and

measured their DOM optical properties and DOC for them at the stations (Fig. 1).

2.2 CDOM

We transferred each sample from a spigot of a Niskin bottle to acid and detergent-cleaned 250-mL plastic bottles after three rinses. We then filtered the CDOM samples using 0.2-μm Nuclepore polycarbonate filters, which we rinsed with Milli-Q water before use. The samples were then stored in the dark in a refrigerator until analysis. After the samples were acclimated to the ambient laboratory temperature in the dark, we measured the absorbance spectra of the filtrates onboard between 190 and 600 nm at 0.5-nm intervals in 10-cm pathlength quartz cuvettes using a UV–Vis recording spectrophotometer (UV-2600, Shimadzu Co.). The measurements were taken within one day of sampling. We measured absorbance spectra of samples and blanks (Milli-Q water) against the reference Milli-Q water. To correct baseline offsets in the measurements, we subtracted the value at 600 nm from the entire absorbance spectrum of each sample (Yamashita et al. 2013).

2.3 FDOM

We transferred each sample from a spigot of a Niskin bottle through a pre-combusted GF/F filter into pre-combusted glass vials with acid-washed Teflon-lined caps after triple rinsing. We stored the samples in the dark in a refrigerator until analysis. We measured the spectra of EEM fluorescence onboard using the method described by Shigemitsu et al. (2020). Briefly, emission scans at 248–829 nm were obtained at 2.33-nm intervals for sequential excitations at 240–560 nm at 5-nm intervals, with an integration time of 12 s and using the high charge-coupled device (CCD) gain mode. The measurements were taken within two days of sampling. Furthermore, we converted the spectra to Raman units (RU) using the Milli-Q water spectra obtained on every EEM measurement day (Lawaetz and Stedmon 2009). Here, we did not apply inner filter effect correction because the absorption coefficients of seawater samples in this study were much lower (i.e., 1.00 ± 0.16 m^{-1} at 250 nm) than the threshold of 10 m^{-1} for the correction (Stedmon and Bro 2008).

2.4 DOC

We obtained seawater samples for DOC analyses following the same method as used for FDOM, except for the sample collection bottles. For DOC, we used acid-washed 60-mL high-density polyethylene bottles. Upon sample collection, we immediately froze the bottles until analysis. In the land laboratory at JAMSTEC, we thawed the frozen samples at room temperature and acidified them

to pH < 2 with hydrochloric acid following the method of Wakita et al. (2016). We then measured DOC using a Shimadzu TOC-L system coupled with a Shimadzu Total N analyzer. We checked the accuracy of the DOC measurements on each DOC measurement day using reference materials provided by D. A. Hansell (University of Miami, USA). All the measurements of Florida Strait reference waters (700 m) yielded results of 42.4 ± 2.7 µmol kg^{-1} ($n = 66$) across all sample measurements. The precision was estimated from the standard deviation of duplicate measurements and was within 2.4 µmol kg^{-1}.

2.5 Chlorophyll *a*
We obtained seawater samples for chlorophyll *a* (Chl a) from the surface to 250 m. We transferred each sample from a spigot of a Niskin bottle to a detergent-washed 250 or 500-mL brown plastic bottle without headspace. Upon collection, we gently filtered the samples under low vacuum pressure (< 0.02 MPa) through a GF/F filter in a dark room, followed by pigment extraction in 7 mL of N,N-dimethylformamide in the dark at − 20 ℃ for > 24 h. We measured Chl a concentrations using an onboard Turner fluorometer (10-AU-005, TURNER DESIGNS).

2.6 Data treatment
We calculated the CDOM absorption coefficient at wavelength λ (a_λ (m^{-1})) from the measured absorbance spectrum (A_λ): $a_\lambda = 2.303 \times A_\lambda / l$, where l is the path length of the cuvette (0.1 m). We used four optical parameters to investigate the CDOM quantity and quality. We used a_{254} and a_{325} as proxies for CDOM quantity (Loginova et al. 2016; Iuculano et al. 2019) and calculated the spectral slope coefficient between 275 and 295 nm ($S_{275-295}$) and the ratio of absorption coefficients at 254 nm and 365 nm ($a_{254/365}$) according to Helms et al. (2008) and Engelhaupt et al. (2003), respectively, as proxies of the CDOM quality. The precision estimated from the standard deviation of duplicate measurements for each parameter, a_{254}, a_{325}, $S_{275-295}$, and $a_{254/365}$, was within 0.02 m^{-1}, 0.01 m^{-1}, 0.001 nm^{-1}, and 0.62, respectively.

We analyzed the obtained EEMs ($n = 946$) using PARA-FAC. The PARAFAC modeling was performed using the eem_parafac function in the staRdom library for R (version 3.6.1). For the PARAFAC analysis, we used the EEMs for excitation wavelengths ranging from 260 to 450 nm and emission wavelengths ranging from 300 to 550 nm. Each EEM was normalized to its total signal according to the method described by Murphy et al. (2013). The three-component model (C1–C3) was validated by split-half analysis (Murphy et al. 2013). We used the PARA-FAC analysis results as proxies for FDOM quantity. In addition, we calculated the humification index (HIX) (Zsolnay et al. 1999) and biological/autochthonous index

(BIX) (Huguet et al. 2009) and used them as proxies of the FDOM quality. We calculated HIX and BIX by dividing a peak area between 435 and 480 nm by that between 300 and 345 nm (both at excitation 254 nm) and by dividing fluorescence intensity at 380 nm by that at 430 nm (both at excitation 310 nm), respectively. The precision estimated from the standard deviation of duplicate measurements for C1, C2, C3, BIX, and HIX was within 0.0002 RU, 0.0002 RU, 0.0007 RU, 0.16, and 0.10, respectively. At all the stations, duplicate samples for FDOM were collected at 50 m depth.

2.7 Factor analysis
Factor analysis is a statistical method used to obtain a smaller number of latent variables (i.e., common factors) to explain the variability in observed variables, rather than the total number of observed variables, which facilitates the interpretation of observed data (Davis 1973; Glover et al. 2011). The factor model is expressed as follows:

$$Z = AF + E, \tag{1}$$

where **Z** is an $n \times m$ data matrix (where n is the number of variables, and m is the number of samples); **A** is an $n \times p$ matrix of factor loadings (where p is the number of factors); **F** is a $p \times m$ matrix of factor scores; and **E** is an $n \times m$ error matrix. Assuming that no correlations exist between the factor scores for each factor, between errors for each variable, or between factor scores and errors, the following equation can be introduced:

$$R = AA' + V, \tag{2}$$

where **R** is the variance–covariance matrix for variables; **A**$'$ is the transposed **A**; and **V** is the variance–covariance matrix for errors. **A** is estimated to reproduce **R** as much as possible, and the factor scores, **F**, can be estimated as follows: $F = Z' R^{-1} A$, where R^{-1} is the inverse of **R**. Factor loading represents the extent to which each variable is associated with each factor, and the factor score is the amount of each factor that is specific to each sample.

For factor analysis, we used the quantity and quality parameters of CDOM, FDOM (a_{254}, a_{325}, $S_{275-295}$, $a_{254/365}$, the sum of C1 and C2, C3, BIX, and HIX), and DOC obtained within the surface mixed layer ($n = 56$) after all the parameters were standardized. Factor analysis was conducted with the varimax rotation of factors using R (version 4.0.3).

2.8 Other relevant data
We determined three factors via factor analysis. To gain new insights from the results, we obtained and used the monthly mean net primary production (NPP) from the

Oregon State Ocean Productivity Website (http://orca.science.oregonstate.edu/npp_products.php), monthly means of ultraviolet (UV) radiation (specific output called "downward UV radiation at the surface") from the ERA5 reanalysis (Hersbach et al. 2020), monthly climatological temperature and salinity data from the World Ocean Atlas 2013 (Locarnini et al 2013; Zweng et al. 2013), and daily sea ice concentration (AMSR-2) from the EUMETSAT website (https://osi-saf.eumetsat.int/products/osi-408). For NPP, we used the averages of the four satellite-derived NPP products: (1) vertically generalized productivity model (VGPM) (Behrenfeld and Falkowski 1997); (2) Eppley-VGPM model (Eppley 1972; Behrenfeld and Falkowski 1997); (3) carbon, absorption, and fluorescence euphotic-resolving model (CAFE) (Silsbe et al. 2016); and (4) carbon-based productivity model (CbPM) (Westberry et al 2008). For the temperature and salinity data, we calculated the monthly climatological mixed layer depth, which is the depth at which a density increases from the sea surface value and exceeds $0.125\ \sigma_\theta$.

3 Results and discussion

3.1 Meridional distributions of potential temperature, salinity, and Chl *a*

From INDW to SSTC, potential temperature and salinity in the surface mixed layer generally decreased from ~ 32 to ~ 13 °C and increased from ~ 32.5 to ~ 35.5, respectively, with decreasing latitude (Additional fig 1: Figs. S1a and b). In INDW and northern MONS, low-salinity water (~ 32.5 to ~ 34.0) was prominent, and in the season when the observations were obtained, these areas would be influenced by the Northeast Monsoon Current (NMC) and North Equatorial Current (NEC), which has low salinity, being derived from BoB and waters transported westward through the Indonesian archipelago (Longhurst 1998). In southern MONS and northern ISSG, salinity was lower and the potential temperature was higher than that in the southern ISSG. The water in the southern MONS and northern ISSG provinces is affected by the South Equatorial Current (SEC), which has relatively low salinity (Longhurst 1998; Talley and Sprintall 2005). SSTC lies between the subtropical and subantarctic waters; consequently, the potential temperature and salinity in this province are between the values of the ISSG and SANT. From SANT to APLR, potential temperature and salinity in the surface mixed layer decreased from ~ 13 to − 2 °C and remained relatively constant (~ 33.5–34), respectively. SANT is located in the Antarctic Circumpolar Current (ACC), the ANTA province is located between the polar front and the Antarctic divergence, and the APLR province is in the most polar region from the coast of Antarctica to the north of the Antarctic divergence (Longhurst 1998).

The Chl *a* concentrations in the surface mixed layer in INDW, MONS, and ISSG decreased from ~ 1 to ~ 0.04 µg L^{-1} with decreasing latitude and were generally lower than the subsurface maxima of Chl *a* below the surface mixed layer (Additional fig 1: Fig. S1c). In the SSTC to ANTA provinces, the Chl *a* concentrations in the surface mixed layer decreased from ~ 1.5 to ~ 0.2 µg L^{-1} with decreasing latitude. We found higher values in the provinces but not below the surface mixed layer, which was different to that in INDW, MONS, and ISSG. In APLR, the Chl *a* concentrations in the surface mixed layer were much lower than those in SANT and ANTA, and the subsurface Chl *a* maxima were present as in INDW, MONS, and ISSG.

3.2 Meridional distributions of DOM quantity proxies

We obtained three components using PARAFAC analysis of the EEMs (Additional fig 1: Fig. S2). The two humic-like components (C1 and C2) and one protein-like component (C3) are comparable to those reported by Kim et al. (2020) in the whole water column along the transect of 67° E, covering 5° N to 16° S in the Indian Ocean. Our results are also comparable to those of Yamashita et al. (2017) for the Pacific Ocean and of Catalá et al. (2015a, b) and Jørgensen et al. (2011) for the global ocean. C1 showed peaks at the excitation/emission pair of 260/474 nm and 365/474 nm for the primary and secondary peaks, respectively; C2 had peaks at the pair of 260/393 nm and 320/393 nm for the primary and secondary peaks, respectively. C3 had peaks at the excitation/emission pair of 265/352 nm as the primary peak and is considered a tryptophan-like component.

DOC, a_{254}, and C3 in the surface mixed layer showed similar spatial distributions (Fig. 2a, b, f; Table 1). From the northernmost INDW to the southernmost APLR provinces, these levels gradually decreased, with small maxima in SSTC and around its borders (ISSG to the north and SANT to the south). These parameters ranged from ~ 88 µmol kg^{-1} to ~ 38 µmol kg^{-1}, from ~ 1.6 m^{-1} to ~ 0.8 m^{-1}, and from 0.023 RU to 0.005 RU, respectively. The vertical aspects of DOC, a_{254}, and C3 generally tended to decrease with depth (Figs. 3a, b, and 4c), except that C3 tended to have maxima below the surface mixed layer from INDW to ISSG, the tendency of which was similar to that of Chl *a*. The vertical trends in DOC and a_{254} were similar to those reported in previous studies (Hansell 2009; Iuculano et al. 2019), and those of C3, including the subsurface maxima, are also similar to previous observations (Catalá et al. 2016; Makarewicz et al. 2018).

The distribution of C1 in the surface mixed layer was similar to that of C2, as also indicated in previous studies (Fig. 2d, e; Table 1) (Catalá et al. 2016; Yamashita
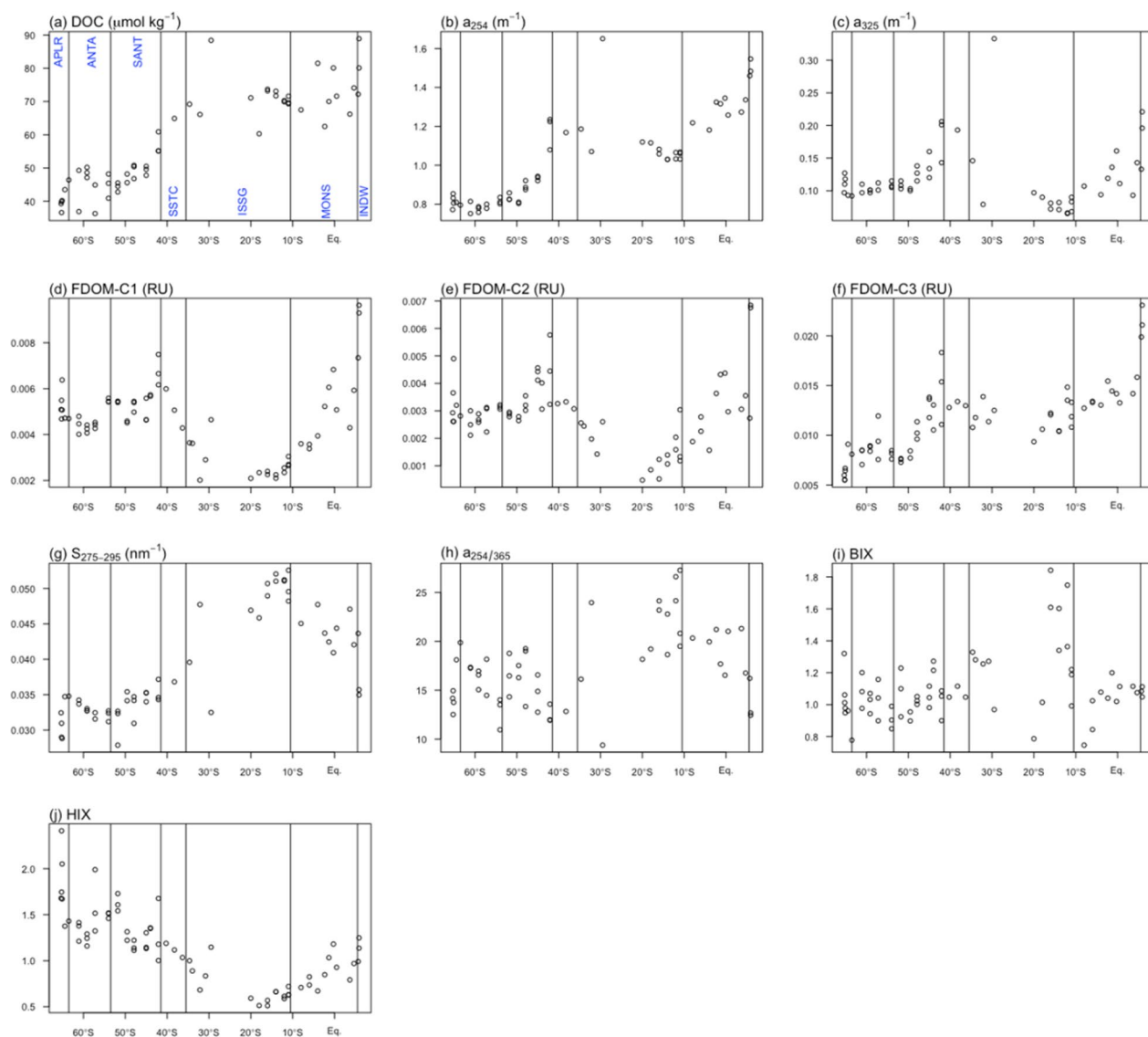
Fig. 2 Meridional distributions in the surface mixed layer of **a** DOC (μmol kg^{-1}), **b** a_{254} (m^{-1}), **c** a_{325} (m^{-1}), **d** FDOM-C1 (RU), **e** FDOM-C2 (RU), **f** FDOM-C3 (RU), **g** $S_{275-295}$ (nm^{-1}), **h** $a_{254/365}$, **i** BIX, and **j** HIX. All data from the surface mixed layer are shown. Large variations in some variables at individual stations are due to (1) relatively close distance between stations (instances in INDW and APLR) or (2) relatively low vertical sampling resolution (10, 50, 100, 150, 200, and 250 m as well as Chl *a* maximum depth), resulting in some sampling depths being positioned near the bottom of the surface mixed layer and a Chl *a* maximum depth potentially being included in the layer. Vertical lines show each boundary between the biogeochemical provinces

et al. 2017). Both distributions showed the highest values (~ 0.010 RU for C1 and ~ 0.007 RU for C2) in INDW and decreased to the lowest values (~ 0.002 RU for C1 and ~ 0.001 RU for C2) in ISSG, with the small maxima in MONS. From ISSG to the south, the values again increased to the second highest values (~ 0.007 RU for C1 and ~ 0.006 RU for C2) around the border between SSTC and SANT, followed by a gradual decrease (to ~ 0.004 RU for C1 and ~ 0.003 RU for C2) to ANTA, and sharp increases (to ~ 0.006 RU for C1 and ~ 0.005 RU for C2)

from ANTA to APLR. The C1 and C2 levels generally tended to increase with depth (Fig. 4a, b), which is consistent with the values reported in previous studies (Jørgensen et al. 2011; Catalá et al. 2016; Shigemitsu et al. 2021).

The distribution of a_{325} in the surface mixed layer was also similar to that of C1 and C2 (Fig. 2c; Table 1), with values ranging from ~ 0.08 m^{-1} to 0.20 m^{-1}, except for an extremely high value of ~ 0.32 m^{-1}. a_{325} generally increased with depth, and the depth distribution was also

Table 1 Correlation coefficients between each pair of observed variables in the surface mixed layer

	a_{254}	a_{325}	C1	C2	C3	$S_{275-295}$	$a_{254/365}$	BIX	HIX
DOC	**0.86**[***]	0.27[*]	− 0.08	− 0.09	**0.74**[***]	**0.70**[***]	0.32[*]	0.36[**]	− **0.72**[***]
a_{254}		0.58[***]	0.27[*]	0.21	**0.84**[***]	0.43[***]	− 0.01	0.12	− 0.47[***]
a_{325}			0.61[***]	0.56[***]	0.43[***]	− 0.40[**]	− **0.70**[***]	− 0.28[*]	− 0.20
C1				**0.88**[***]	0.35[**]	− 0.58[***]	− 0.67[***]	− 0.40[**]	0.54[***]
C2					0.36[**]	− 0.54[***]	− 0.61[***]	− 0.29[*]	0.51[***]
C3						0.39[**]	0.05	0.17	− 0.51[***]
$S_{275-295}$							0.78[***]	0.54[***]	− **0.87**[***]
$a_{254/365}$								0.47[***]	− 0.65[***]
BIX									− 0.41[**]

Absolute values of correlation coefficient greater than or equal to 0.7 are indicated in bold. * $p < 0.05$, ** $p < 0.01$, and *** $p < 0.001$. Dissolved organic carbon (DOC), CDOM absorption coefficient at wavelength λ (a_λ (m^{-1})), components determined using PARAFAC analysis (C1–C3), spectral slope coefficient between 275 and 295 nm ($S_{275-295}$), absorption coefficient ratio at 254 and 365 nm ($a_{254/365}$), biological index (BIX), and humification index (HIX)

similar to that of C1 and C2 (Figs. 3c, 4a, b) and to the trend reported in previous studies (Catalá et al. 2016; Iuculano et al. 2019).

3.3 Meridional distributions of DOM quality proxies
The distribution of $S_{275-295}$ in the surface mixed layer was similar to that of $a_{254/325}$ (Fig. 2g, h; Table 1). Both parameters had the highest values in the northern ISSG (~ 0.050 nm^{-1} for $S_{275-295}$ and ~ 27 for $a_{254/325}$), which decreased in both the northward and southward directions. In the southward direction, they reached minimum values (~ 0.030 nm^{-1} for $S_{275-295}$ and ~ 11 for $a_{254/325}$) around the border between SANT and ANTA, followed by increases to around the border between ANTA and APLR and sharp decreases in APLR. They generally tended to decrease with depth (Fig. 5a, b), which is consistent with the findings of a previous study (Iuculano et al. 2019).

To the best of our knowledge, BIX has not been previously reported in basin-scale observations. BIX in the surface mixed layer generally showed a similar trend to $S_{275-295}$ and $a_{254/365}$, except for the absence of a gradual decrease from ISSG to MONS and a sharp decrease in APLR (Fig. 2g–i; Table 1). This reflects a weaker correlation between BIX and $S_{275-295}$ or between BIX and $a_{254/325}$ compared to that between $S_{275-295}$ and $a_{254/325}$. The BIX values ranged from approximately 0.8–1.8. The vertical distributions of BIX were complicated (Fig. 5c). In INDW, northern MONS, and ISSG, BIX decreased with depth with subsurface maxima similar to that of Chl *a* concentrations; whereas, in the other BGCPs, BIX increased or remained relatively constant with depth.

The HIX in the surface mixed layer showed opposite trends in $S_{275-295}$, $a_{254/365}$, and BIX, i.e., HIX had the lowest values of ~ 0.5 in the northern ISSG, which increased to ~ 1.1 and ~ 2.2 in both the northward and southward directions, respectively (Fig. 2g–j; Table 1). The southward increase involved a small maximum of ~ 1.7 around the border between SANT and ANTA. The vertical distribution was opposite to those of $S_{275-295}$, $a_{254/365}$, and BIX and generally increased with increasing depth (Fig. 5d), which is consistent with observations in the Atlantic (Kowalczuk et al. 2013).

3.4 Interpretation of factor analysis results
When conducting factor analysis, we used the sum of the humic-like components C1 and C2 as an original variable because both the spatial distributions were similar, as stated above. In terms of determining the number of factors in this study, we selected the factors which explained > 10% of the variance. We identified three factors in this study: the first, second, and third factors explained 37.9%, 36.0%, and 10.1% of the variance, respectively, with a total of approximately 84%. The uniqueness of each variable, showing the proportion of variance that could not be explained by the three factors, was 8.9% for DOC, 6.4% for a_{254}, 16.7% for C3, 1.3% for a_{325}, 0.5% for the sum of humic-like components, 3.6% for $S_{275-295}$, 19.2% for $a_{254/365}$, 71.1% for BIX, and 16.7% for HIX. From the results, BIX was the least explained by the three factors; hence, we found no strong correlations between BIX and other variables (Table 1).

In a factor analysis, the factor loadings show the extent to which each observed variable is related with each factor (Fig. 6). Factor 1 (F1) showed large positive loadings for DOC, a_{254}, and C3, and a negative loading for HIX. Factor 2 (F2) showed large positive loadings for $a_{254/365}$ and $S_{275-295}$ and large negative loadings for a_{325}, HIX, and the sum of the humic-like components (T-humic). Factor 3 (F3) showed a large positive and negative loading for T-humic and $S_{275-295}$, respectively.
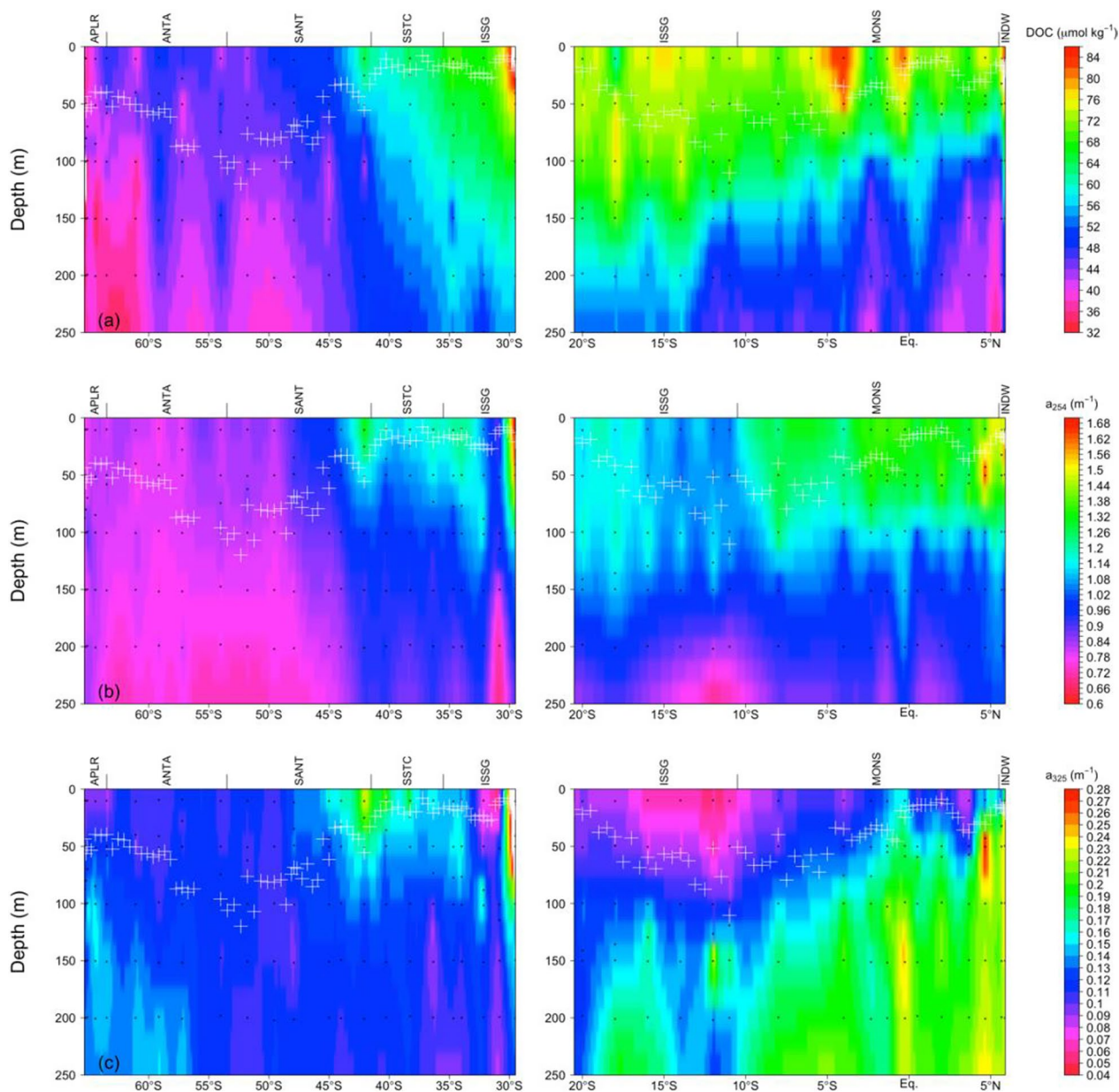
Fig. 3 Meridional distributions of **a** DOC (µmol kg^{-1}), **b** a_{254} (m^{-1}), and **c** a_{325} (m^{-1}). Right and left columns represent Leg 2 and 3 transects, respectively. White plus signs represent the mixed layer depths, which we calculated as the depth at which a density increase from the sea surface value was > 0.125 σ_θ

F1 accounted for the biogeochemical process that had a stronger influence on DOC, a_{254}, and C3 than HIX (Fig. 6a). DOC and protein-like C3 in surface waters are mainly derived from primary production in surface waters (Castillo et al. 2010; Brym et al. 2014; Makarewicz et al. 2018; Moran et al. 2022). In addition, those parameters tend to have the similar vertical distributions, i.e., high levels in the surface water and decreasing with depth (Hansell et al. 2009; Kowalczuk et al. 2013), which

is consistent with our findings (Figs. 3a and 4c). a_{254} is considered to be a proxy for DOC (Catalá et al. 2018; Iuculano et al. 2019). a_{254} in the surface mixed layer was significantly correlated with the DOC concentrations in this study (Table 1) and showed similar vertical distributions to those of DOC (Fig. 3a, b). Conversely, according to Zsolnay et al. (1999), HIX increases with humification, i.e., the higher the HIX, the older the DOM. If primary production is closely related to F1, autochthonously
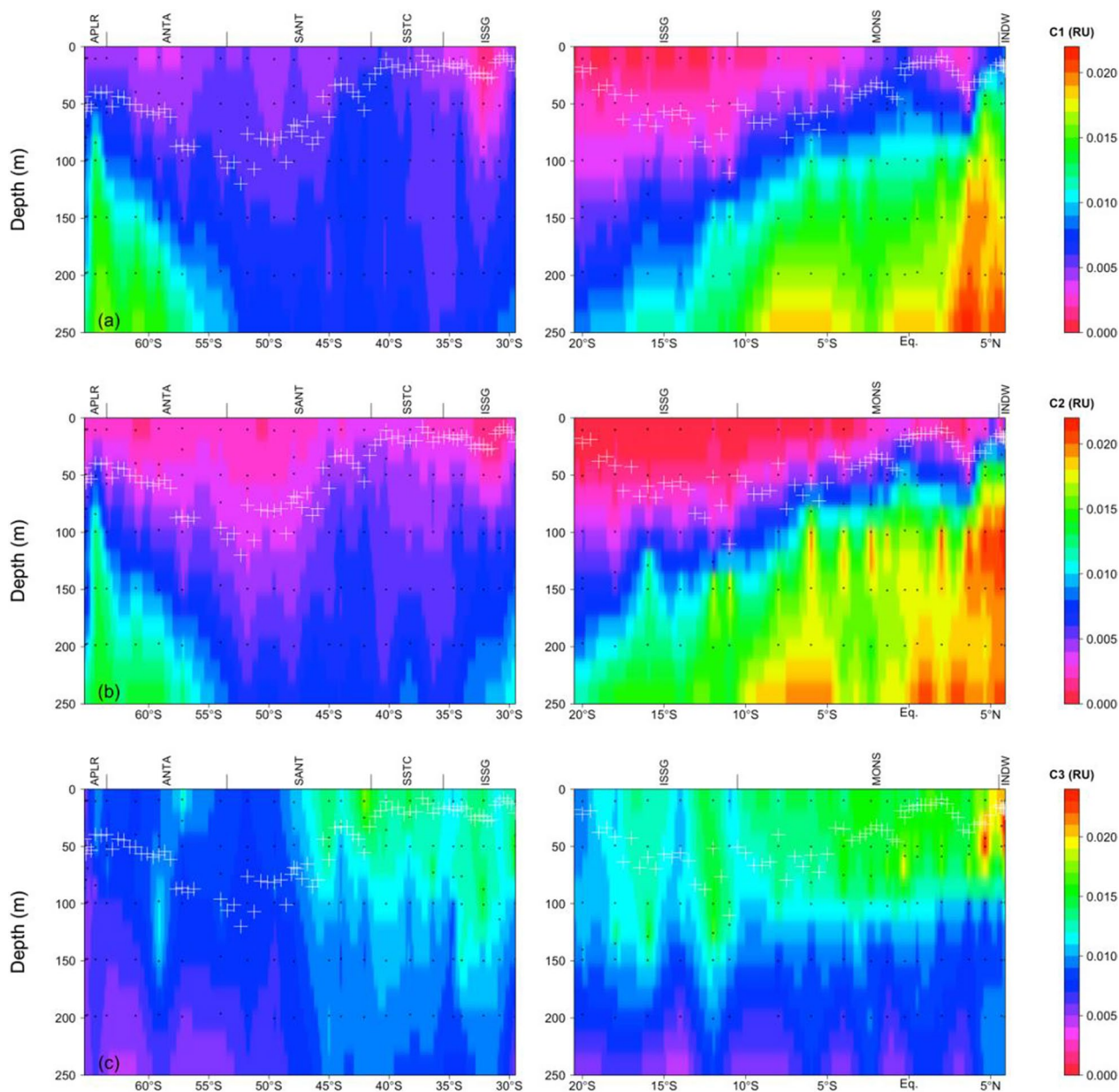
Fig. 4 Meridional distributions of **a** FDOM-C1 (RU), **b** FDOM-C2 (RU), and **c** FDOM-C3 (RU). The definitions of the right and left columns and white plus signs are the same as in Fig. 3

produced DOM in the surface mixed layer should be fresher, resulting in low HIX values (or high DOC, a_{254}, and C3 levels). One caveat should be observed in this interpretation. HIX calculation used the areas under the curve of emission 300–345 nm at excitation 254 nm, and the C3 levels might have affected the HIX levels (Fig. S2). However, the correlation coefficient between HIX and C3 was weaker than that between HIX and DOC and between HIX and $S_{275-295}$ (Table 1). Thus, the effect of C3 on HIX was minimal. In this context, F1 was interpreted

as the effect of surface primary production on DOM. This conclusion is corroborated by the following aspects. DOM in surface waters can be decomposed by solar radiation (Catalá et al. 2016), which is called photodegradation. However, solar radiation has less influence on DOC and protein-like C3 than on humic-like components (Mostofa et al. 2007). a_{254} is also less influenced by photodegradation than a_{325} (Iuculano et al. 2019) because a_{325} is a proxy for aromatic substances produced by heterotrophic prokaryotes that absorb UVA radiation
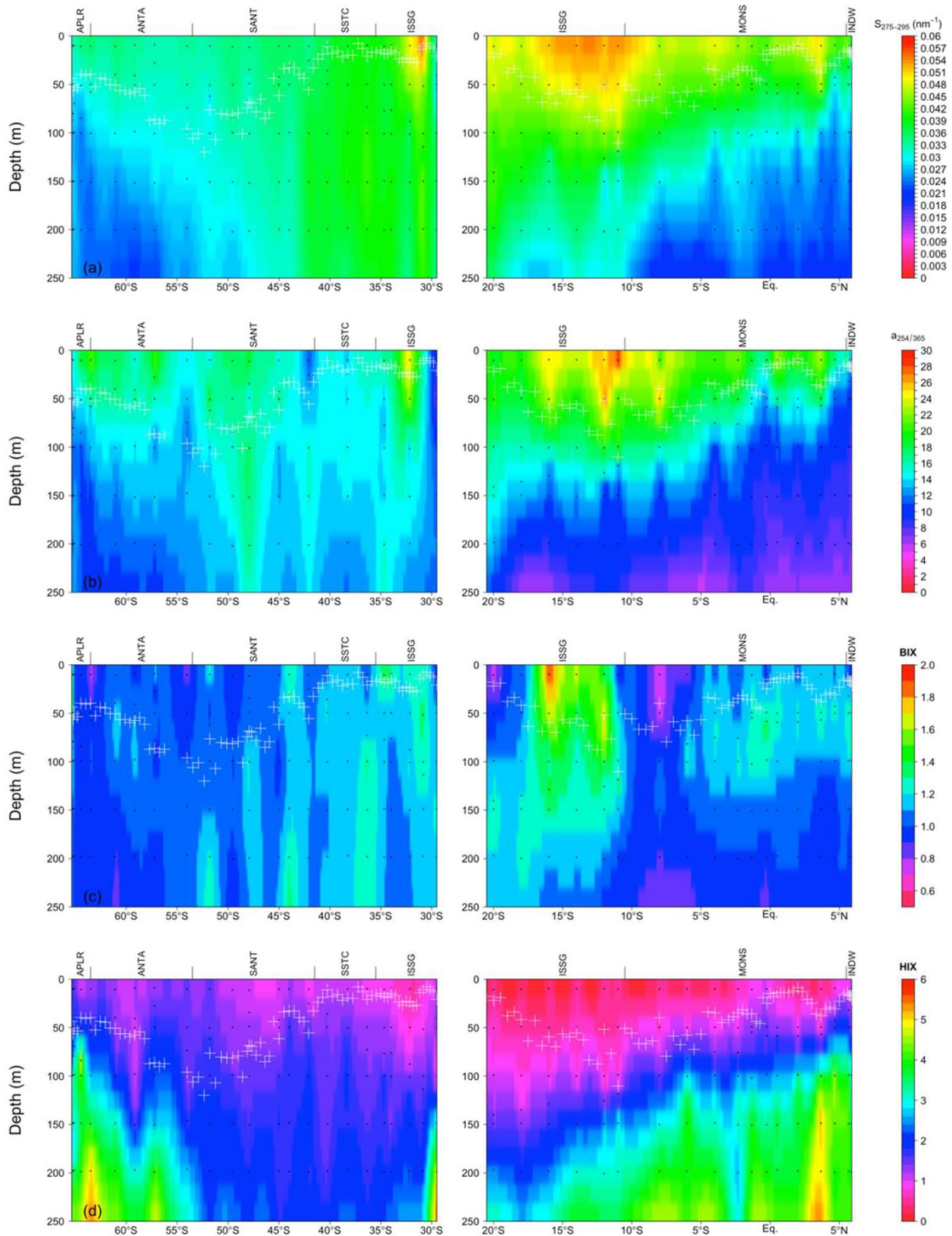
Fig. 5 Meridional distributions of **a** $S_{275-295}$ (nm^{-1}), **b** $a_{254/365}$, **c** BIX, and **d** HIX. The definitions are the same as in Fig. 3
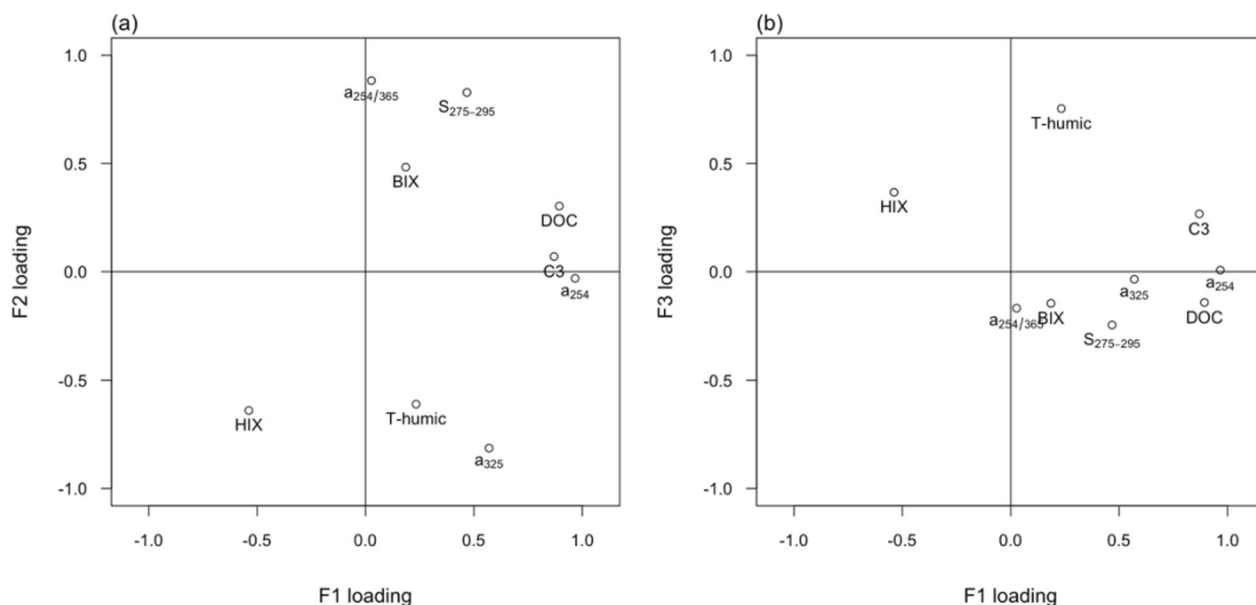
Fig. 6 Scatter plots of **a** factor loadings of F1 vs. F2 and **b** of F1 vs. F3. T-humic, the sum of humic-like C1 and C2

and are subject to photodegradation (Nelson et al. 2004; Catalá et al. 2018). This results in the rarity of significant positive correlations between a_{325} and DOC (Nelson and Siegel 2013), which applied to our findings (Fig. 3a, c; Table 1). Although primary producers generate humic-like components (Castillo et al. 2010), photodegradation influences humic-like components, resulting in low levels in surface waters (Omori et al. 2010). Thus, considering the extent to which photodegradation affect the DOM parameters, the result whereby T-humic and a_{325} showed the smaller positive loadings compared to DOC, a_{254}, and C3 is reasonable.

Regarding F2, $a_{254/365}$, and $S_{275-295}$, which showed large positive loadings, are related to the effect of photodegradation and the molecular weight of DOM (Dahlén et al. 1996; Helms et al. 2008). Their parameter values increase as photodegradation affects DOM (Obernosterer and Herndl 2000; Helms et al. 2008), whereas the lower the molecular weight of the DOM, the higher the values of both parameters, and vice versa. As stated above, a_{325} and humic-like components are subject to photodegradation. Thus, when DOM undergoes photodegradation, the a_{325} and T-humic values decrease and the $a_{254/365}$ and $S_{275-295}$ values increase. Furthermore, Helms et al. (2013) and Hansen et al. (2016) indicated that HIX and BIX decreased and increased, respectively, with photodegradation. From these perspectives, it is evident that F2 can be interpreted as the effect of photodegradation on DOM.

Regarding F3, the vertical distributions of humic-like components with a large positive loading generally increased with depth, whereas those of $S_{275-295}$ with a large negative loading generally decreased with depth (Figs. 4a, b, and 5a). Especially in INDW, APLR, around the border between SSTC and SANT, and near the equator, the levels of both C1 and C2 in and just below the surface mixed layer were higher than those in the neighboring regions (Figs. 2d, e, 4a, b). In contrast, the levels of $S_{275-295}$ for APLR in and below the surface mixed layer were lower than those in the other BGCPs, and the values in INDW, around the border between SANT and ANTA, and near the equator, had local minimum values (Figs. 2g and 5a). If T-humic and $S_{275-295}$ in the surface mixed layer are affected by vertical physical processes, such as advection, mixing, and entrainment, the former tends to increase and the latter tends to decrease. Thus, F3 was interpreted as the effect of vertical physical processes on DOM.

One caveat should be observed in interpretations of F2 and F3. The factor loadings of both, except those of C3 and a_{325}, generally showed mutually opposite trends (Fig. 6), obscuring their separability. Variables that were more likely to be affected positively by photodegradation, i.e., $a_{254/365}$ and $S_{275-295}$, tended to decrease with depth (Fig. 5), whereas those that seemed to be predominantly influenced in the direction by vertical physical processes, i.e., T-humic, were apt to increase with depth (Fig. 4). Thus, vertical physical processes might determine the factor loadings of F2 and F3. However, as shown in Sects. 3.5.2 and 3.5.3, the photodegradation degree of DOM in the surface mixed layer is expected to be small in BGCPs, where vertical physical processes exert

a dominant influence on the surface DOM, but large in BGCPs, where this influence is not predominant. The geographically based difference in magnitude between possible effects of photodegradation and vertical physical processes on the surface DOM probably enables us to separate F2 from F3. In addition, as noted in Sect. 3.2, C3 generally decreased with depth but showed subsurface maxima from INDW to ISSG, making it possible for C3 to positively contribute to F3; in contrast, C3 had no influence on F2 at all (Fig. 6). These results also corroborate a possible separation of F2 from F3 based on the present observations. Although a_{325} generally increases with depth, the variable does not contribute to F3 at all, which is probably due to its relatively noisy geographical distribution in the surface mixed layer.

3.5 Comparison of each factor score and relevant environmental parameter

We determined three factors using factor analysis and interpreted each factor based on both the factor loadings assigned to the observed variables and the characteristics of the variables (Fig. 6). F1 was the effect of primary production on DOM, and F2 and F3 were the effects of photodegradation and vertical physical processes (i.e., advection, mixing, and entrainment) on DOM, respectively. Here, we compared the spatial distribution of each factor score (Fig. 7) with the related environmental parameter (Fig. 8) to gain deeper insights into the DOM dynamics in the surface waters.

3.5.1 F1: Effect of primary production on DOM

The monthly averaged NPP interpolated to each station for each satellite-derived NPP product (i.e., local NPP) in November 2019, December 2019, and January 2020 was similar in spatial distribution and magnitude; the exception was CAFE-based NPP in BoB, which showed the opposite trend (Additional fig 1: Fig. S3). The similarities among the products applied to the annually averaged local NPP and zonally and annually averaged NPP (20°–100° E). Thus, we considered the average of four

satellite NPP products to be the representative NPP in the Indian Ocean (Fig. 8a).

The monthly averages of local NPP were relatively similar in spatial distribution to the F1 scores ($r = 0.80$, $n = 52$, $p < 0.001$; using the NPP data in December for Leg 2 and in January for Leg 3; in the calculation, NPP of each station was assigned to all associated samples), except that the NPP values in MONS and INDW were lower than those from the northern SANT to SSTC (Figs. 7a and 8a). Although the trends in the annual mean of local NPP and zonally and annually averaged NPP (20°–100° E) were similar to those of the monthly averages, the NPP values for the formers were more similar to the distribution of F1 scores than the monthly averaged local NPP ($r = 0.92$, $n = 52$, $p < 0.001$; $r = 0.89$, $n = 56$, $p < 0.001$; in the calculation, NPP of each station was assigned to all associated samples) (Figs. 7a and 8a). Notably, the annual mean of local NPP, and zonally and annually averaged NPP (20°–100° E) in MONS and INDW showed higher or similar values than or to those from the northern SANT to SSTC, respectively. From the results, we concluded that the annually averaged local NPP or zonally and annually averaged NPP represented the F1 scores. This may mean that the meridional distribution of DOM in the surface mixed layers, which is related to surface NPP, is determined on an annual time scale.

In addition to NPP, horizontal transport of NPP-derived DOM may also contribute to the F1 score distribution. In the season when the MR19-04 cruise was conducted, the northeast (NE) monsoon, which occurs from December–April, is conventionally predominant. The NE monsoon generates the Northeast Monsoon Current (NMC), which flows from the BoB through INDW and northern MONS to AS (Schott et al. 2009; De Vos et al. 2014). Because the surface salinities in the BoB are lower than those in the INDW and northern MONS on the transect considered in this study (Akhil et al. 2016), the observed low salinities in INDW and northern MONS would be affected by NMC (Additional fig 1: Fig. S1b). This suggested that DOM which
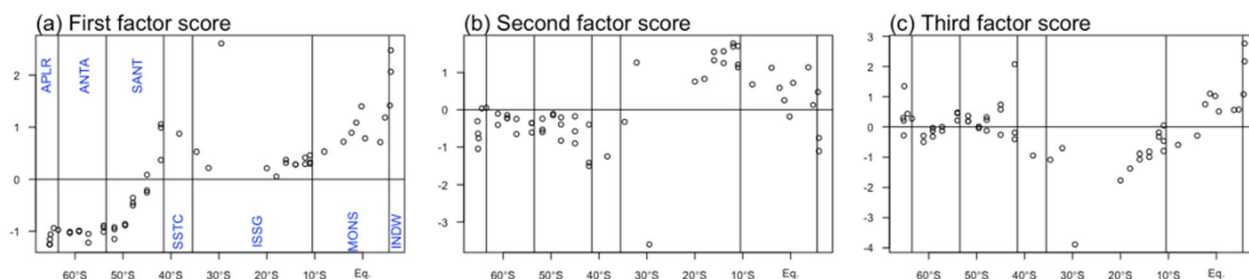
Fig. 7 Meridional distributions of factor scores of **a** F1, **b** F2, and **c** F3. As in Fig. 2, all data in the surface mixed layer are shown. Vertical lines show the boundaries between the biogeochemical provinces
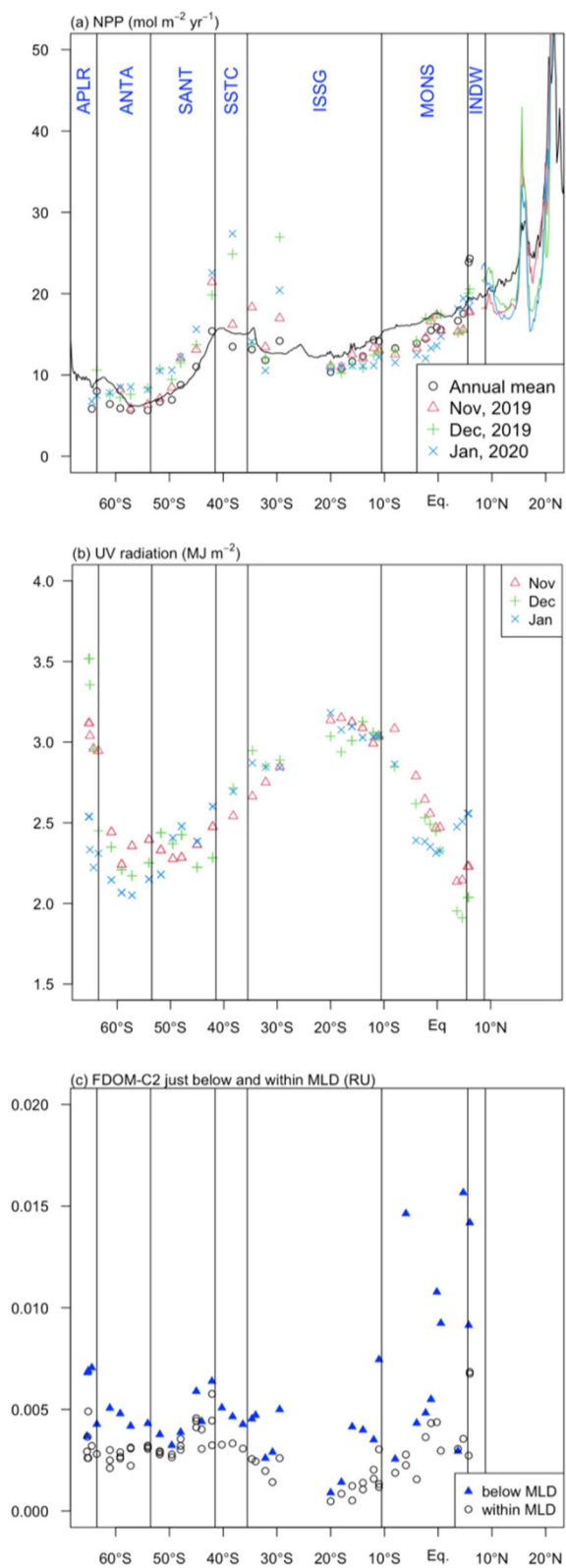
Fig. 8 Meridional distributions of **a** NPP (mol m^{-2} year^{-1}), **b** UV radiation (MJ m^{-2}), and **c** FDOM-C2 (RU). **a** Red triangles, green plus signs, and blue crosses represent the monthly averaged NPP of four NPP model outputs (VGPM, Eppley-VGPM, CAFÉ, and CbPM) interpolated for each station in November 2019, December 2019, January 2020, respectively; black circles are annually averaged NPP of four NPP model outputs interpolated for each station during period from February 2019 to January 2020. Red, green, and blue lines are the monthly and zonally averaged NPP of four NPP models in the Bay of Bengal in November 2019, December 2019, and January 2021, respectively; black line is the zonally (20° E–100° E) and annually averaged NPP of four NPP models from February 2019 to January 2020. **b** Colored symbols have the same meaning as in **a** except that they represent the UV radiation data. **c** Blue solid triangles and black open circles represent C2 levels just below and in the surface mixed layer, respectively. Vertical lines in each panel show the boundaries between the biogeochemical provinces. MLD: mixed layer depth. Note that the *x*-axis of each panel is expanded to the north in a different manner than in Figs. 2 and 7 and that the boundary of INDW is indicated by a vertical line as in those figures

was produced and/or existed in the BoB was transported to the regions of the transect. In the BoB, NPP was much higher than that in INDW and northern MONS throughout a year (Fig. 8a) and the DOC concentrations in the surface waters of the BoB would also be higher than those in INDW and northern MONS. Thus, the horizontal transport of DOM via NMC would also contribute to shaping the F1 score distribution in INDW and northern MONS. Considering that the annually averaged NPP is more influential in the distribution of F1 scores than monthly mean NPP, the southwest monsoon current (SMC), which flows from the AS through INDW and northern MONS into the BoB during the southwest (SW) monsoon season (June–October), may also affect the DOM in the surface waters of INDW and northern MONS (Schott et al. 2009; De Vos et al. 2014). That is because the zonally and annually averaged NPP in AS was much higher than that in INDW and northern MONS (Fig. 8a). Finally, as stated in Sect. 3.1, the zonal currents, such as NEC and SEC, would also affect the F1 score distribution. However, taking it into account that "annually averaged local NPP" and "zonally and annually averaged NPP" were similar in spatial distribution to each other, the effect would be relatively small.

Taken together, we found that F1 represented the effect of "annually averaged local NPP" or "zonally and annually averaged NPP" and its horizontal transport on DOM. The effect of horizontal transport of DOM on the meridional distribution in the surface waters of the Indian Ocean should be quantitatively confirmed in future studies.

3.5.2 F2: Effect of photodegradation on DOM

The UV radiation (UVR) interpolated to each station (i.e., local UVR) in November 2019, December 2019, and January 2020 had maximum values in the northern ISSG, which decreased from there in both northward and southward directions. In the southward direction, the UVR had minimum values in SANT to ANTA and increased values from ANTA to APLR. The UVR distribution was significantly correlated with that of the F2 scores ($r = 0.62$, $n = 49$, $p < 0.001$; using the UVR data in December for Leg 2 and in January for Leg 3; in the calculation, UVR of each station was assigned to all associated samples) except for stations in APLR and with an extremely negative F2 score in ISSG (Figs. 7b and 8b). The reason behind the weak correlation between UVR and F2 scores would derive from the fact that UVR is known to have a small e-folding depth for the attenuation with depth in water and the e-folding depth varies from clear to turbid waters (Tedetti and Sempere 2006). The uppermost samples for DOM in this study were obtained at approximately 10 m depth along the two transects, and the difference in UVR e-folding depth between stations is considered to be important for determining the correlation.

In APLR, F2 scores decreased and UVR increased. In APLR, even in January 2020 when the observations were obtained, sea ice covered the province to some extent (Fig. 9). Thus, the effect of UVR should be attenuated by the sea ice cover and the trends in F2 score and UVR in APLR would be the opposite to each other. In addition, APLR includes the Antarctic divergence, and the residence time of the surface waters would be short, which is considered to be the cause of the locally lower

Fig. 9 Averaged sea ice concentration (%) in the vicinity of Antarctica from January 1, 2020, to January 22, 2020, on which sampling stations (white open circles) are superimposed

anthropogenic CO_2 content (Sarmiento and Gruber 2006). If the residence time of the surface water is short, the period of DOM exposure to sunlight is also short. Thus, the short residence time of surface water also influenced the difference between the F2 scores and UVR in APLR. The timescale on which photodegradation influences the surface DOM distribution is unclear in this study and should be studied in future.

3.5.3 F3: Effect of vertical physical transport processes on DOM

We obtained the optical properties of DOM and DOC during a single cruise; therefore, estimating the contribution of each vertical physical transport process to surface DOM optical properties and DOC was difficult. As stated above, the variable with a large positive loading in F3 was T-humic, and the variable with a large negative loading was $S_{275-295}$ (Fig. 6). Thus, for humic-like components, the transport into the surface mixed layer by vertical mixing, advection, and entrainment would tend to increase the levels of humic-like components in this layer. The humic-like C2 levels just below the surface mixed layer (C1 was similar to C2 and is not shown here) were generally higher than those within the mixed layer depth, and the latitudinal distributions just below and within the surface mixed layer were similar (Fig. 8c). Thus, if humic-like components are supplied into the surface mixed layer from below, the levels in the surface mixed layer increase.

A picture of vertical advection driven by divergent Ekman flow has been shown in the previous studies (Liang et al. 2017; Nagura and McPhaden 2018). The vertical advection by Ekman pumping was upward in INDW, MONS and APLR, but was downward in ISSG through SSTC to SANT. These results are consistent with the F3 score distribution (Fig. 7c). In addition, to obtain information regarding the effect of entrainment, we investigated the climatological mixed layer depths along the occupied transects in this study. The climatological mixed layer depths in INDW and MONS deepen twice a year, i.e., from November–December to January–February and from March–April to June–September (Fig. 10). The climatological mixed layer depths in the SW monsoon (June–October) are deeper than those in the NE monsoon (December–April). In INDW and MONS, the deepest climatological mixed layer depth was approximately 40 m in depth and the effect of entrainment on DOM in the surface mixed layer would be the largest in INDW and around the equator because the C1 and C2 levels at this depth were the highest in INDW and MONS (Fig. 4a, b). This is also consistent with the F3 score distribution. In ISSG to APLR, the climatological mixed layer depths monotonically increased from December–February (austral summer) to July–September (austral winter).
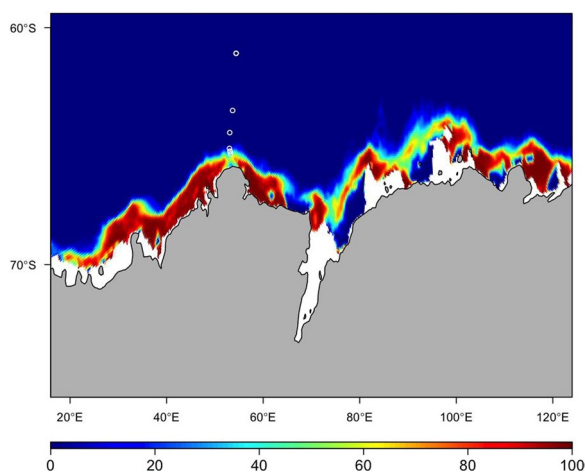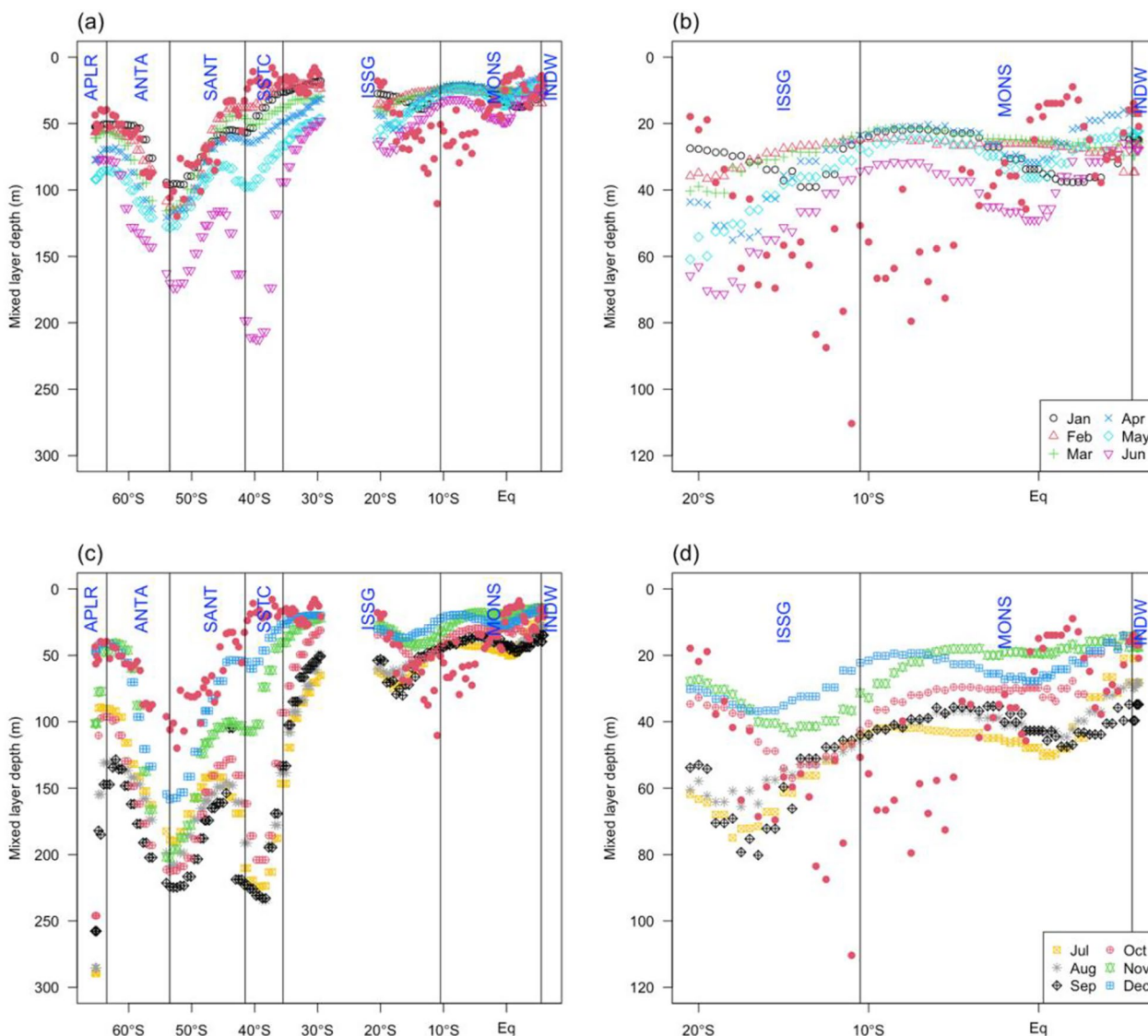
Fig. 10 **a**, **c** Climatological monthly mixed layer depth (m) calculated from temperature and salinity of World Ocean Atlas 2013 for the periods of January–June and for July–December, respectively. We simply calculated mixed layer depth as the depth at which a density increase from the sea surface value was > 0.125 σ_θ. Red solid circles represent observations in this study. **b**, **d** As in (**a**, **c**), except for along Leg 2 transect and expanded *y*-axis

In particular, in SSTC, around the border between SANT and ANTA, and APLR, the climatological mixed layers become deepest in austral winter. From SANT to APLR, the isolines of high humic-like component levels (C1 and C2) below the mixed layer depth in austral summer tilted toward the south (Fig. 4a, b). Thus, the effect of entrainment would become higher from SSTC through around the border between SANT and ANTA toward APLR, which is also consistent with the F3 scores. Although estimating the effect of mixing from the results from a single cruise was difficult, the qualitative information regarding the effects of advection and entrainment was

consistent with the F3 score distribution. One caution must be raised again. In Sect. 3.4, separating F2 from F3 in our analysis may have been difficult. We calculated the correlation coefficient between the UVR and F3 score distributions under the same conditions as for between the UVR and F2 score distributions in Sect. 3.5.2. The result was $r = -0.58$; the absolute value was weaker than that between the UVR and F2 score distributions (0.62). Although this is consistent with our interpretation of F2 and F3, the slight difference cannot completely prove the separation of F2 and F3. Thus, quantitative estimation of vertical physical transport of DOM by each process into

the surface mixed layer as well as the time scale on which the DOM level in the surface mixed layer is influenced by each physical process are required in future studies. Finally, when we conducted the observations in this study, a positive Indian Ocean Dipole (IOD) event had occurred (Kouketsu et al. 2022). The observed mixed layer depths in INDW, MONS and ISSG were much deeper than the climatological maximum mixed layer depths at many stations (Fig. 10). Thus, it is notable that the F3 contributions in INDW, MONS, and ISSG may be higher than those in normal conditions or during a negative IOD event.

3.6 Potential interaction between photodegradation, autochthonous production, and bacterial reworking of DOM

We used the correlation structure of the observed variables to obtain common factors with factor analysis. Unlike principal component analysis, contributions that are not explained by common factors are allowed and are called uniqueness (as shown above). Thus, variables with unusual variability are not included as common factors.

Among the observed variables, the uniqueness of BIX was the highest (71.1%); in other words, BIX could not be explained by the common factors, which could be understood from the spatial distribution being dissimilar to those of the common factors (Figs. 2i and 7; and Table 1). We observed high BIX values in the northern ISSG, together with high values of $S_{275-295}$ and $a_{254/365}$ and lower values of HIX, humic-like components, and a_{325} (Fig. 2). Helms et al. (2013) and Hansen et al. (2016) demonstrated that BIX values of subtropical Pacific water collected at ~700 m depth and algae-leachate increased with photo-exposure times of 68 days and 111 days, respectively. The high BIX values in the northern ISSG, where the F2 effect was highest, and the BIX contribution to F2 loading are, therefore, in line with previous studies to some extent. However, both of the long-term photo-exposure experiments showed BIX value increases of approximately 0.2. This extent is much smaller than the latitudinal variation range (0.4–1.0) observed in the surface mixed layer in this study across all the BGCPs, even taking the measurement precision of BIX into account. Additional mechanisms might, therefore, be needed to explain these observations. A higher BIX indicates an increase in DOM levels which have recently been autochthonously produced and reworked by heterotrophic prokaryotes (Huguet et al. 2009; Loginova et al. 2016). Our findings might, therefore, indicate that photodegradation of both of freshly produced and aged DOM was occurring, high-molecular-weight DOM was converted to low-molecular-weight DOM or less aromatic forms, and the low-molecular-weight DOM was reworked by

heterotrophic prokaryotes, resulting in younger DOM, which is consistent with fresher DOM as inferred from the low HIX, humic-like components, and a_{325} values.

Coupling between photodegradation, autochthonous production, and bacterial reworking of DOM is important for understanding the fate of surface DOM because DOM can be converted to CO_2 by these processes, and the generated CO_2 influences the air–sea gas exchange of CO_2 (Kieber et al. 1997; Cory and Kling 2018). However, the interactions in the open ocean are not well known. Our findings indicate the possibility that large-scale, simultaneous observations of the optical properties of DOM and DOC are useful for understanding the interaction between the photodegradation, autochthonous production, and bacterial reworking of DOM.

3.7 Characterizing each biogeochemical province with score of each factor

Three major factors were responsible for most of the variability in optical properties of DOM and DOC: annually averaged local NPP or zonally and annually averaged NPP-derived DOM and its horizontal transport (F1) explained 37.9% of the variance; DOM consumption by photodegradation (F2) explained 36.0%; and vertical transport of DOM by physical processes (F3) explained 10.1%. Each BGCP was characterized by the factor scores (Fig. 7; Table 2).

F1 scores gradually decreased from INDW to APLR, with a local maximum in SSTC and around the border between SSTC and SANT (Fig. 7a; Table 2). SANT is located in the circumpolar ACC, which is bounded to the north by the subtropical front and to the south by the polar front and includes two different ecological zones (Longhurst 1998). Thus, F1 scores in the northern parts of the SANT were high and those in the southern part were low, which resulted in low average F1 scores in the BGCP (Fig. 7a; Table 2). F2 scores were high in ISSG

Table 2 Averaged factor scores with standard deviations for each biogeochemical province

Province	F1	F2	F3
INDW	1.99 ± 0.54	− 0.46 ± 0.83	2.00 ± 0.86
MONS	0.91 ± 0.29	0.56 ± 0.47	0.45 ± 0.60
ISSG	0.48 ± 0.62	0.87 ± 1.39	− 1.02 ± 0.95
SSTC	0.87	− 1.24	− 0.94
SANT	− 0.29 ± 0.70	− 0.57 ± 0.45	0.26 ± 0.61
ANTA	− 1.01 ± 0.09	− 0.33 ± 0.18	− 0.03 ± 0.32
APLR	− 1.10 ± 0.14	− 0.44 ± 0.45	0.38 ± 0.54

Western India Coastal (INDW), Indian Monsoon Gyres (MONS), Indian South Subtropical Gyre (ISSG), South Subtropical Convergence (SSTC), Subantarctic Water Ring (SANT), Antarctic (ANTA), Austral Polar (APLR), and factor analysis factors 1–3 (F1–F3)

and MONS, with decreasing trends from there in both the northward and southward directions. The high photodegradation of DOM in the subtropical region, ISSG, is in line with that previously observed in the Atlantic (Kowalczuk et al. 2013) (Fig. 7b; Table 2). F3 scores were high in INDW, MONS, and APLR, in agreement with upward Ekman pumping (Liang et al. 2017; Nagura and McPhaden 2018) and the presumed entrainment discussed above (Fig. 7c). F3 scores were low in ISSG, which is also consistent with downward Ekman pumping (Liang et al. 2017; Nagura and McPhaden 2018).

Overall, each BGCP was characterized by the three factors that were determined by factor analysis. This indicated that the effects of various biogeochemical processes, including physical processes, on DOM in the surface mixed layer are closely related to the BGCPs determined based on the geographical patterns of phytoplankton ecology and biogeochemical characteristics (Longhurst 1998).

4　Conclusions

In this study, we investigated the meridional distributions of the optical properties of DOM and DOC in the Indian Ocean. Using these observations, we conducted factor analysis to extract the common factors that explained the distributions. Consequently, we identified three factors: annually averaged local NPP or zonally and annually averaged NPP-derived DOM and its horizontal transport (F1); DOM consumption by photodegradation (F2); and vertical transport of DOM by physical processes (F3). The observed variables are generally related to primary production, except for a_{325} that is related to heterotrophic prokaryote production. The extent to which these parameters were affected by photodegradation differed. The difference in photoreactivity dependence and origin among the observed variables led to differences in the spatial distributions of the observed variables and helped with extracting the three common factors. Although BIX could not be explained by these factors, their spatial distributions led to the additional information that DOM reworked by heterotrophic prokaryotes and autochthonously produced existed in the northern part of ISSG and that the photo- and biodegradation of DOM interacted. In addition, the difference in spatial distribution between F2 scores and UVR in APLR indicated that DOM photodegradation should be prevented by sea ice cover. Our findings demonstrated that the multiproxy approach based on the optical properties of DOM and DOC is a powerful tool for examining marine DOM dynamics.

Abbreviations

ANTA	Antarctic
APLR	Austral polar
BGCP	Biogeochemical province
BIX	Biological index
CDOM	Chromophoric dissolved organic matter
DOC	Dissolved organic carbon
DOM	Dissolved organic matter
EEM	Excitation emission matrices
FDOM	Fluorescent dissolved organic matter
HIX	Humification index
INDW	Western India Coastal
ISSG	Indian South Subtropical Gyre
MONS	Indian Monsoon Gyres
NEC	North equatorial current
NMC	Northeast monsoon current
NPP	Net primary productivity
PARAFAC	Parallel factor analysis
RU	Raman units
SANT	Subantarctic water ring
SEC	South equatorial current
SSTC	South subtropical convergence
UV	Ultraviolet
UVR	Ultraviolet radiation

Supplementary Information

The online version contains supplementary material available at https://doi.org/10.1186/s40645-024-00623-0.

> **Additional file 1**. Supplementary figures.

Author contributions

MS and KS measured FDOM, DOC, and CDOM. MS conducted the analyses for the results and prepared the manuscript based on advice from KS, MW, TY, TH, KA, and AM. All authors read and approved the final manuscript.

Availability of data and materials

Monthly net primary production data were available from the Oregon State Ocean Productivity website (http://orca.science.oregonstate.edu/npp_products.php). Monthly means of UV radiation are available from the ERA5 reanalysis data (https://cds.climate.copernicus.eu/cdsapp#!/dataset/reanalysis-era5-single-levels?tab=form). Monthly climatological temperature and salinity data are from the World Ocean Atlas 2013 (https://www.nodc.noaa.gov/OC5/SELECT/woaselect/woaselect.html), and daily sea ice concentration (AMSR-2) are from the EUMETSAT website (https://osi-saf.eumetsat.int/products/osi-408). The data of DOM presented in this study are available from the corresponding author upon reasonable request.

Declarations

Competing interests

The authors declare that they have no competing interest.

References

Akhil VP, Lengaigne M, Durand F, Vialard J, Chaitanya AVS, Keerthi MG, Gopalakrishna VV, Boutin J, de Boyer MC (2016) Assessment of seasonal and year-to-year surface salinity signals retrieved from SMOS and Aquarius missions in the Bay of Bengal. Int J Remote Sens 37:1089–1114. https://doi.org/10.1080/01431161.2016.1145362

Andrews SS, Caron S, Zafiriou OC (2000) Photochemical oxygen consumption in marine waters: a major sink for colored dissolved organic matter? Limnol Oceanogr 45:267–277

Behrenfeld MJ, Falkowski PG (1997) Photosynthetic rates derived from satellite-based chlorophyll concentration. Limnol Oceanogr 42:1–20

Bertilsson S, Tranvik LJ (1998) Photochemically produced carboxylic acids as substrates for freshwater bacterioplankton. Limnol Oceanogr 43:855–895

Broek TAB, Walker BD, Guilderson TP, Vaughn JS, Mason HE, McCarthy MD (2020) Low molecular weight dissolved organic carbon: aging, compositional changes, and selective utilization during global ocean circulation. Global Biogeochem Cycles 34:GB006547. https://doi.org/10.1029/2020GB006547

Brym A, Paerl HW, Montgomery MT, Handsel LT, Ziervogel K, Osburn CL (2014) Optical and chemical characterization of base-extracted particulate organic matter in coastal marine environments. Mar Chem 162:96–113. https://doi.org/10.1016/j.marchem.2014.03.006

Castillo CR, Sarmento H, Álvarez-Salgado XA, Gasol JM, Marraséa C (2010) Production of chromophoric dissolved organic matter by marine phytoplankton. Limnol Oceanogr 55:446–454. https://doi.org/10.4319/lo.2010.55.1.0446

Catalá TS, Álvarez-Salgado XA, Otero J, Iuculano F, Companys B, Horstkotte B, Romera-Castillo C, Nieto-Cid M, Latasa M, Morán XAG, Gasol JM, Marrasé C, Stedmon CA, Reche I (2016) Drivers of fluorescent dissolved organic matter in the global epipelagic ocean. Limnol Oceanogr 61:1101–1119. https://doi.org/10.1002/lno.10281

Catalá-Pérez AM, Martínez-Pérez AM, Nieto-Cid M, Álvarez M, Otero J, Emelianov M, Reche I, Arístegui J, Álvarez-Salgado XA (2018) Dissolved organic matter (DOM) in the open Mediterranean Sea. I. Basin-wide distribution and drivers of chromophoric DOM. Prog Oceanogr 165:35–51. https://doi.org/10.1016/j.pocean.2018.05.002

Catalá TS, Reche I, Álvarez M, Khatiwala S, Guallart EF, Benítez-Barrios VM, Fuentes-Lema A, Romera-Castillo C, Nieto-Cid M, Pelejero C, Fraile-Nuez E, Ortega-Retuerta E, Marrasé C, Álvarez-Salgado XA (2015a) Water mass age and aging driving chromophoric dissolved organic matter in the dark global ocean. Global Biogeochem Cycles 29:917–934. https://doi.org/10.1002/2014GB005048

Catalá TS, Reche I, Fuentes-Lema A, Romera-Castillo C, Nieto-Cid M, Ortega-Retuerta E, Calvo E, Álvarez M, Marrasé C, Stedmon CA, Álvarez-Salgado XA (2015b) Turnover time of fluorescent dissolved organic matter in the dark global ocean. Nat Commun 6:5986. https://doi.org/10.1038/ncomms6986

Cory RM, Kling GW (2018) Interactions between sunlight and microorganisms influence dissolved organic matter degradation along the aquatic continuum. Limnol Oceanogr Lett 3:102–116. https://doi.org/10.1002/lol2.10060

Dahlén J, Bertilsson S, Pettersson C (1996) Effects of UV-A irradiation on dissolved organic matter in humic surface waters. Environ Int 22:501–506. https://doi.org/10.1016/0160-4120(96)00038-4

Davis JC (1973) Statistics and data analysis in geology. Wiley, New York

De Vos A, Pattiaratchi CB, Wijeratne EMS (2014) Surface circulation and upwelling patterns around Sri Lanka. Biogeosciences 11:5909–5930. https://doi.org/10.5194/bg-11-5909-2014

del Giorgio PA, Duarte CM (2002) Respiration in the open ocean. Nature 420:379–384

Engelhaupt E, Bianchi TS, Wetzel RG, Tarr MA (2003) Photochemical transformations and bacterial utilization of high-molecular-weight dissolved organic carbon in a southern Louisiana tidal stream (Bayou Trepagnier). Biogeochemistry 62:39–58

Eppley RW (1972) Temperature and phytoplankton growth in the sea. Fish Bull 70:1063–1085

Glover DM, Jenkins WJ, Doney SC (2011) Modeling methods for marine science. Cambridge University Press, Cambridge

Hansell DA (2009) Dissolved organic carbon in the carbon cycle of the Indian Ocean. Geophys Monogr S 185:217–230. https://doi.org/10.1029/2007GM000684

Hansell DA (2013) Recalcitrant dissolved organic carbon fractions. Ann Rev Mar Sci 5:421–445. https://doi.org/10.1146/annurev-marine-120710-100757

Hansell DA, Carlson CA, Repeta DJ, Schlitzer R (2009) Dissolved organic matter in the ocean: a controversy Stimulates new insights. Oceanography 22:202–211. https://doi.org/10.5670/oceanog.2009.109

Hansell DA, Carlson CA, Schlitzer R (2012) Net removal of major marine dissolved organic carbon fractions in the subsurface ocean. Glob Biogeochem Cycles 26:GB1016. https://doi.org/10.1029/2011GB004069

Hansen AM, Kraus TEC, Pellerin BA, Fleck JA, Downing BD, Bergamaschi BA (2016) Optical properties of dissolved organic matter (DOM): effects of biological and photolytic degradation. Limnol Oceanogr 61:1015–1032

Heller MI, Gaiero DM, Croot PL (2013) Basin scale survey of marine humic fluorescence in the Atlantic: relationship to iron solubility and H_2O_2. Global Biogeochem Cycles 27:88–100. https://doi.org/10.1029/2012GB004427

Helms JR, Stubbins A, Ritchie JD, Minor EC (2008) Absorption spectral slopes and slope ratios as indicators of molecular weight, source, and photobleaching of chromophoric dissolved organic matter. Limnol Oceanogr Methods 53:955–969

Helms JR, Stubbins A, Perdue EM, Green NW, Chen H, Mopper K (2013) Photochemical bleaching of oceanic dissolved organic matter and its effect on absorption spectral slope and fluorescence. Mar Chem 155:81–91

Hersbach H, Bell B, Berrisford P, Hirahara S, Horányi A, Muñoz-Sabater J, Nicolas J, Peubey C, Radu R, Schepers D, Simmons A, Soci C, Abdalla S, Abellan X, Balsamo G, Bechtold P, Biavati G, Bidlot J, Bonavita M, Chiara G, Dahlgren P, Dee D, Diamantakis M, Dragani R, Flemming J, Forbes R, Fuentes M, Geer A, Haimberger L, Healy S et al (2020) The ERA5 global reanalysis. QJR Meteorol Soc 146:1999–2049

Huguet A, Vacher L, Relexans S, Saubusse S, Froidefond JM, Parlanti E (2009) Properties of fluorescent dissolved organic matter in the Gironde Estuary. Org Geochem 40:706–719. https://doi.org/10.1016/j.orggeochem.2009.03.002

Iuculano F, Álverez-Salgado XA, Otero J, Catalá TS, Sobrino C, Duarte CM, Agustí S (2019) Patterns and drivers of UV absorbing chromophoric dissolved organic matter in the euphotic layer of the open ocean. Front Mar Sci 6:320. https://doi.org/10.3389/fmars.2019.00320

Jørgensen L, Stedmon CA, Kragh T, Markager S, Middelboe M, Søndergaard M (2011) Global trends in the fluorescence characteristics and distribution of marine dissolved organic matter. Mar Chem 126:139–148. https://doi.org/10.1016/j.marchem.2011.05.002

Kawasaki N, Benner R (2006) Bacterial release of dissolved organic matter during cell growth and decline: Molecular origin and composition. Limnol Oceanogr 51:2170–2180

Kieber RJ, Hydro LH, Seaton PJ (1997) Photooxidation of triglycerides and fatty acids in seawater: implication toward the formation of marine humic substances. Limnol Oceanogr 42:1454–1462

Kim J, Kim Y, Kang H-W, Kim SH, Rho T, Kang D-J (2020) Tracing water mass fractions in the deep western Indian Ocean using fluorescent dissolved organic matter. Mar Chem 218:103720. https://doi.org/10.1016/j.marchem.2019.103720

Kouketsu S, Murata A, Arulananthan K (2022) Subsurface water property structures along 80°E under the positive Indian Ocean Dipole mode in December 2019. Front Mar Sci 9:848756

Kowalczuk P, Tilstone GH, Zabłocka M, Röttgers R, Thomas R (2013) Composition of dissolved organic matter along an Atlantic meridional transect from fluorescence spectroscopy and parallel factor analysis. Mar Chem 157:170–184. https://doi.org/10.1016/j.marchem.2013.10.004

Lampert W (1978) Release of dissolved organic carbon by grazing zooplankton. Limnol Oceanogr 23:831–834

Lawaetz AJ, Stedmon CA (2009) Fluorescence intensity calibration using the Raman scatter peak of water. Appl Spectrosc 63:936–940

Liang X, Spall M, Wunsch C (2017) Global ocean vertical velocity from a dynamically consistent ocean state estimate. J Geophys Res Oceans 122:8208–8224. https://doi.org/10.1002/2017JC012985

Locarnini RA, Mishonov AV, Antonov JI, Boyer TP, Garcia HE, Baranova OK, Zweng MM, Paver CR, Reagan JR, Johnson DR, Hamilton M, Seidov D (2013) World ocean atlas 2013 temperature. S. Levitus Mishonov A ed, vol. 1 Technical Ed.; NOAA Atlas NESDIS 73, p 40

Loginova AN, Thomsen S, Engel A (2016) Chromophoric and fluorescent dissolved organic matter in and above the oxygen minimum zone off Peru. J Geophys Res Oceans 121:7973–7990. https://doi.org/10.1002/2016JC011906

Lønborg C, Nieto-Cid M, Hernando-Morales V, Hernandez-Ruiz M, Teira E, Álvarez-Salgado XA (2016) Photochemical alteration of dissolved organic matter and the subsequent effects on bacterial carbon cycling and diversity. FEMS Microbiol Ecol 92:Fiw048. https://doi.org/10.1093/femsec/fiw048

Lønborg C, Carreira C, Jickells T, Álvarez-Salgado XA (2020) Impacts of global change on ocean dissolved organic carbon (DOC) cycling. Front Mar Sci 7:466. https://doi.org/10.3389/fmars.2020.00466

Longhurst AR (1998) Ecological geography of the sea. Academic Press, Cambridge

Makarewicz A, Kowalczuk P, Sagan S, Granskog MA, Pavlov AK, Zdun A, Borzycka K, Zabłocka M (2018) Characteristics of chromophoric and fluorescent dissolved organic matter in the Nordic Seas. Ocean Sci 14:543–562. https://doi.org/10.5194/os-14-543-2018

Medeiros PM, Seidel M, Powers LC, Dittmar T, Hansell DA, Miller WL (2015) Dissolved organic matter composition and photochemical transformations in the northern North Pacific Ocean. Geophys Res Lett 42:863–870. https://doi.org/10.1002/2014GL062663

Middelboe M, Lyck PG (2002) Regeneration of dissolved organic matter by viral lysis in marine microbial communities. Aquat Microb Ecol 27:187–194

Miller WL, Zepp RG (1995) Photochemical production of dissolved inorganic carbon from terrestrial organic matter: significance to the oceanic organic carbon cycle. Geophys Res Lett 22:417–420

Møller EF (2007) Production of dissolved organic carbon by sloppy feeding in the copepods Acartia tonsa, Centropaages typicus, and Temora longicornis. Limnol Oceanogr 52:79–84

Moran MA, Ferrer-Gonzalez FX, Fu H, Nowinski B, Olofsson M, Powers MA, Schreier JE, Schroer WF, Smith CB, Uchiyama M (2022) The ocean's labile DOC supply chain. Limnol Oceangr. https://doi.org/10.1002/lno.12053

Moran MA, Sheldon WM Jr, Zepp RG (2000) Carbon loss and opticalaa property changes during long-term photochemical and biologicala degradation of estuarine dissolved organic matter. Limnol Oceanogr 45:1254–1264

Mostofa KMG, Yoshioka T, Konohira E, Tanoue E (2007) Photodegradation of fluorescent dissolved organic matter in river waters. Geochem J 41:323–331

Murphy KR, Stedmon CA, Graeber D, Bro R (2013) Fluorescence spectroscopy and multi-way techniques. PARAFAC Anal Methods 5:6557–6556. https://doi.org/10.1039/c3ay41160e

Nagura M, McPhaden MJ (2018) The shallow overturning circulation in the Indian Ocean. J Phys Oceanogr 48:413–434. https://doi.org/10.1175/JPO-D-17-0127.1

Nelson NB, Carlson CA, Steinberg DK (2004) Production of chromophoric dissolved organic matter by Sargasso Sea microbes. Mar Chem 89:273–287

Nelson NB, Siegel DA (2013) The global distribution and dynamics of chromophoric dissolved organic matter. Ann Rev Mar Sci 5:447–476. https://doi.org/10.1146/annurev-marine-120710-100751

Obernosterer I, Benner R (2004) Competition between biological and photochemical processes in the mineralization of dissolved organic carbon. Limnol Oceanogr 49:117–124

Obernosterer I, Herndl GJ (2000) Differences in the optical and biological reactivity of the humic and nonhumic dissolved organic carbon component in two contrasting coastal marine environments. Limnol Oceanogr 45:1120–1129

Omori Y, Hama T, Ishii M, Saito S (2010) Relationship between the seasonal change in fluorescent dissolved organic matter and mixed layer depth in the subtropical western North Pacific. J Geophys Res 115:C06001. https://doi.org/10.1029/2009JC005526

Roshan S, DeVries T (2017) Efficient dissolved organic carbon production and export in the oligotrophic ocean. Nat Commun 8:2036. https://doi.org/10.1038/s41467-017-02227-3

Sarmiento JL, Gruber N (2006) Ocean biogeochemical dynamics. Princeton University Press, Princeton

Schott FA, Xie SP, McCreary JP (2009) Indian Ocean circulation and climate variability. Rev Geophys 47:RG1002. https://doi.org/10.1029/2007RG000245

Shah C, Sudheer AK, Bhushan R (2018) Distribution of dissolved organic carbon in the Bay of Bengal: influence of sediment discharge, fresh water flux, and productivity. Mar Chem 203:91–101. https://doi.org/10.1016/j.marchem.2018.04.004

Shigemitsu M, Uchida H, Yokokawa T, Arulananthan K, Murata A (2020) Determining the distribution of fluorescent organic matter in the Indian Ocean using in situ fluorometry. Front Microbiol 11:589262

Shigemitsu M, Yokokawa T, Uchida H, Kawagucci S, Murata A (2021) Sedimentary supply of humic-like fluorescent dissolved organic matter and its

implication for chemoautotrophic microbial activity in the Izu-Ogasawara Trench. Sci Rep 11:19006. https://doi.org/10.1038/s41598-021-97774-7

Silsbe GM, Behrenfeld MJ, Halsey KH, Milligan AJ, Westberry TK (2016) The CAFÉ model: a net production model for global ocean phytoplankton. Global Biogeochem Cycles 30:1756–1777

Song G, Li Y, Hu S, Li G, Zhao R, Sun X, Xie H (2017) Photobleaching of chromophoric dissolved organic matter (CDOM) in the Yangtze River estuary: kinetics and effects of temperature, PH, and salinity. Environ Sci Process Impacts 19:861–873

Stedmon CA, Bro R (2008) Characterizing dissolved organic matter fluorescence with parallel factor analysis: a tutorial. Limnol Oceanogr Methods 6:572–579. https://doi.org/10.4319/lom.2008.6.572b

Stedmon CA, Nelson NB (2015) The optical properties of DOM in the Ocean. In: Carlson CA, Hansell DA (eds) Biogeochemistry of marine dissolved organic matter. Academic Press, San Diego, pp 65–126. https://doi.org/10.1016/B978-0-12-405940-5.00003-0

Sumata H, Hashioka T, Suzuki T, Yoshie N, Okunishi T, Aita MN, Sakamoto TT, Ishida A, Okada N, Yamanaka Y (2010) Effect of eddy transport on the nutrient supply into the euphotic zone simulated in an eddy-permitting ocean ecosystem model. J Mar Syst 83:67–87

Talley LD, Sprintall J (2005) Deep expression of the Indonesian throughflow: Indonesian intermediate water in the South equatorial current. J Geophys Res 110:C10009. https://doi.org/10.1029/2004JC002826

Tedetti M, Sempéré R (2006) Penetration of ultraviolet radiation in the marine environment: a review. Photochem Photobiol 82:389–397

Thibodeau PS, Steinberg DK, Maas AE (2020) Effects of temperature and food concentration on pteropod metabolism along the western Antarctic Peninsula. J Exp Mar Biol Ecol 530–531:15142

Veldhuis M, Kraay G, Timmermans K (2001) Cell death in phytoplankton: correlation between changes in membrane permeability, photosynthetic activity, pigmentation and growth. Eur J Phycol 36:167–177

Wakita M, Honda MC, Matsumoto K, Fujiki T, Kawakami H, Yasunaka S, Sasai Y, Sukigara C, Uchimiya M, Kitamura M, Kobari T, Mino Y, Nagano A, Watanabe S, Saino T (2016) Biological organic carbon export estimated from the annual carbon budget observed in the surface waters of the western subarctic and subtropical North Pacific Ocean from 2004 to 2013. J Oceanogr 72:665–685

Westberry T, Behrenfeld MJ, Siegel DA, Boss E (2008) Carbon-based primary productivity modeling with vertically resolved photoacclimation. Global Biogeochem Cycles. https://doi.org/10.1029/2007GB003078

Wood AM, Van Valen LM (1990) Paradox lost? On the release of energy-rich compounds by phytoplankton. Mar Microb Food Webs 4:103–116

Yamashita Y, Hashihama F, Saito H, Fukuda H, Ogawa H (2017) Factors controlling the geographical distribution of fluorescent dissolved organic matter in the surface waters of the Pacific Ocean. Limnol Oceanogr 62:2360–2374

Yamashita Y, Nosaka Y, Suzuki K, Ogawa H, Takahashi K, Saito H (2013) Photobleaching as a factor controlling spectral characteristics of chromophoric dissolved organic matter in open ocean. Biogeosciences 10:7207–7217

Zsolnay A, Baigar E, Jimenez M, Steinweg B, Saccomandi F (1999) Differentiating with fluorescence spectroscopy the sources of dissolved organic matter in soils subjected to drying. Chemosphere 38:45–50

Zweng MM, Reagan JR, Antonov JI, Locarnini RA, Mishonov AV, Boyer TP, Garcia HE, Baranova OK, Johnson DR, Seidov D, Biddle MM (2013) World ocean atlas 2013 Salinity. S. Levitus Mishonov A ed, vol. 2 Technical Ed.; NOAA Atlas NESDIS 74, p 39

Publisher's Note